Journal of Magnetic Resonance 214 (2012) 227–236

Contents lists available at SciVerse ScienceDirect

Journal of Magnetic Resonance

journal homepage: www.elsevier.com/locate/jmr

High spatial resolution NMR imaging of polymer layers on metallic substrates

Haijin Zhu, Hendrik P. Huinink *, Sebastiaan J.F. Erich, Viktor Baukh, Olaf C.G. Adan, Klaas Kopinga

Department of Applied Physics, Transport in Permeable Media, Eindhoven University of Technology, P.O. Box 513, 5600 MB Eindhoven, The Netherlands

ARTICLE INFO

Article history:
Received 6 September 2011
Revised 9 November 2011
Available online 30 November 2011

Keywords:
GARfield NMR
Surface coil
Simulation
Metal
Off-resonance
Eddy current

ABSTRACT

High spatial resolution NMR imaging techniques have been developed recently to measure the spatial inhomogeneity of a polymer coating film. However, the substrates of the polymer coatings for such experiments are generally required to be non-metallic, because metals can interact with static magnetic fields $\mathbf{B_0}$ and RF fields $\mathbf{B_1}$ giving rise to artifacts in NMR images. In this paper we present a systematic study on the effects of metallic substrates on 1D profiles obtained by high resolution NMR imaging. The off-resonance effect is discussed in detail in terms of the excitation profile of the RF pulses. We quantitatively show how the NMR signal intensities change with frequency offset at different RF pulse lengths. The complete NMR profiles were simulated using a Finite Element Analysis method by fully considering the inhomogeneities in both $\mathbf{B_1}$ and $\mathbf{B_0}$. The excellent agreement between the calculated and measured NMR profiles on both metallic and non-metallic substrates indicates that the experimental NMR profiles can be reproduced very well by numerical simulations. The metallic substrates can disturb the RF field of the coil by eddy current effect and therefore change the NMR profiles. To quantitatively interpret the NMR profile of a polymer layer on a metallic substrate, the profile has to be divided by the profile of a reference on the same metallic substrate located at the same distance from the coil.

1. Introduction

Polymer coatings are widely used for purposes of protection, insulation and decoration, etc. The need for a better understanding of the physical and chemical processes by which they are formed is driven by the desire for better material performance and demands for reducing the release of volatile organic compounds into the atmosphere. In order to understand these processes the coating structure has to be visualized in time, which can be done with MRI.

Various MRI approaches have been developed to study thin layers with a high resolution. Stray Field Imaging (STRAFI) was one of the first MRI techniques to reliably provide profiles and images of solids in 1980s [1,2]. It is characterized by the ultrahigh, constant magnetic field gradient intrinsic to the fringe field of a superconducting magnet. One of the advantages of the fringe field gradient is extremely stable. It allows very precise measurements of diffusion coefficients. In many cases, an MRI measurement needs to be performed on a sample which is bulky or unsuitable to be place in a conventional NMR system. This challenge has been met by unilateral NMR magnets. In an unilateral NMR, the NMR sensor which is much smaller than the object is placed near the object to acquire signals from the object volume [3]. One of the disadvantages of the STRAFI technique is that the curvature in the magnet flux across the region of interest in a STRAFI magnet limits the experimental resolution. For this consideration, a new approach, Gradient At Right-angles to the Field NMR (GARField) was developed to improve the magnetic field homogeneity. It was designed on the basis of STRAFI and unilateral concepts [4]. The shape of the magnet pole-pieces are deliberately designed such that it can provide lines of magnetic flux with constant magnitude parallel to the sensitive plane with an orthogonal gradient in the field strength. With this technique a spatial resolution of 5 μm in the vertical direction can be obtained. It is a very powerful technique in probing depth profiles of polymer coatings during curing or solvent-uptake processes, regardless of the optical transparency [5–7].

In many industrial applications, polymer coatings are applied on metallic substrates. The properties of coatings on these substrates may be quite different from non-metallic substrates due to the different interfacial interactions. A high spatial resolution NMR imaging technique offers a possibility to probe structures in the depth direction of a polymer coating [4,8,9]. However, for these measurements, generally, non-metallic substrates are required, because metals can strongly interact with a static magnetic field $\mathbf{B_0}$ and an oscillating magnetic field $\mathbf{B_1}$. Consequently, they create distortion and artifacts in the NMR images. At high magnetic fields of 1.5 T or above, the influence of a metallic substrate may originate from two effects: susceptibility mismatch between the substrate and the polymer layer and eddy currents produced by both the RF pulse and the switching of the gradient current [10–13]. The susceptibility difference between the metallic substrate and the polymer coating causes a local magnetic field inhomogeneity

* Corresponding author.
E-mail address: h.p.huinink@tue.nl (H.P. Huinink).

1090-7807/$ - see front matter © 2011 Elsevier Inc. All rights reserved.
doi:10.1016/j.jmr.2011.11.009

which is proportional to the main magnetic field $\mathbf{B_0}$, resulting in both faster T_2 relaxation and local changes of the precession frequency. The effect of the magnetic susceptibility on the MRI signal has been widely studied. For instance, Lüdeke et al. gave a complete discussion of the susceptibility related effects caused by non-conducting spheres and cylinders [14]. Schenck systematically reviewed the role of magnetic susceptibility in NMR imaging, and shed light on the quantitative use of susceptibility data in NMR imaging [13]. Less attention has been paid to the artifacts induced by eddy currents, although such effects have been reported [10,11].

An eddy current is the current generated in a conductor when it is subjected to a time-varying magnetic field. It can be generated by switching on and off gradient coils [15] and/or by a strong RF pulse from the transmitting coil [16,17]. At a frequency f, the eddy currents flow along the surface with skin depth [11]

$$\delta = (\pi\mu_0\mu\sigma f)^{-1/2}. \quad (1)$$

Here μ_0 is the magnetic permeability of vacuum, μ is the relative magnetic permeability of the material of interest and σ is the electrical conductivity of the material. In case of a 1.5 T MRI system (f_H = 62.5 MHz), the skin depth δ is about 10 μm for aluminum at room temperature. The thickness of the aluminum plates used in this study is about 600 μm. So, eddy currents can only flow in a very thin layer of the metallic substrate. In the case of a metallic substrate with a thickness much larger than the skin depth, both the RF pulse and the NMR signal can be screened completely. The RF inhomogeneity resulting from the eddy currents can lead to a signal decrease or enhancement, depending on the geometry of the metal object and the distance from it. For metals with a high conductivity and a low susceptibility, such as copper and aluminum, the effect of eddy currents dominates over susceptibility artifacts, whereas for materials with a low conductivity and high susceptibility, such as titanium, this effect is small compared to the susceptibility artifacts. The gradient coil generated eddy current effect is not a serious consideration in the GARField NMR because fixed gradients are used. This is a major advantage of the GARField magnet over conventional imaging systems using pulsed gradients.

In order to obtain a high filling factor and a good signal-to-noise ratio (SNR), generally a surface coil is used in GARfield NMR. However, in contrast to conventional volume coils, which are widely used in high-resolution nuclear magnetic resonance of liquid and solid samples, the surface coil produces a rather inhomogeneous RF magnetic field $\mathbf{B_1}$. This makes it difficult to predict the spin evolution because of the spatial variation of pulse flip angles. Besides, GARfield NMR is also characterized by its extremely strong static magnetic field gradient (~40 T/m), which allows for imaging with a very high spatial resolution of about 5 μm in the direction perpendicular to the coating film. When the inhomogeneity of the static field within the sample is comparable with the strength of RF field, off-resonance effects become important.

The goal of this paper is twofold. First, we will model the effect of a non ferromagnetic metallic substrate on the NMR signal intensity. Experimental results are compared with numerical simulations to interpret the NMR imaging signal profiles. Second, we will describe the evolution of the spin magnetization during an Ostroff–Waugh (O–W) type of pulse sequence, $\theta x - \left[\frac{t_E}{2} - \theta_y - \frac{t_E}{2} - echo\right]_n$ with arbitrary flip angle θ [18], in an inhomogeneous RF field and strong off-resonance conditions. And one should note the magnetization has contributions from different coherent pathways [19]. This work extends the application of high-spatial resolution NMR imaging techniques to polymer coatings on metallic substrates. This paper is organized as follows: the first part of Section 2 describes how we simulate the NMR signal using a Finite Element Method (FEM) by fully considering the inhomogeneities in both RF field and static magnetic field. Next, the simulation of the RF field of a surface coil and the induced NMR signal are also described. Section 3 describes the NMR setup, NMR parameters, and the samples used in this study. In Section 4, we first show the effect of magnetic susceptibility on the experimental NMR profiles. Next, the RF field of the surface coil is simulated. Based on this result, NMR signals originating from space voxels and sample slices in y–z planes (Fig. 1) are calculated. Then, complete NMR profiles are simulated in the experimental frequency range and compared with experimental results. Off-resonance effects are discussed in detail in terms of different RF power levels and pulse lengths at the end of Section 4. Finally, in Section 5, we choose the curing process of an epoxy/amine system as an example, to demonstrate the effect of a metallic substrate on the NMR signal in a real system.

2. Theory and numerical simulation

A Finite Element Method (FEM) was used to simulate the NMR signal [20]. The sample was divided into small voxels in space. Both the $\mathbf{B_1}$ field in the voxel and the evolution of the spin magnetization within each voxel were calculated. Finally, the signal induced in the receiver coil by the spins was calculated. The simulation method is described in this section. Unless otherwise stated, the laboratory coordinate frame is defined as follows (Fig. 1): the z direction is along the $\mathbf{B_0}$ field and the x-direction is set perpendicular to the surface coil. The calculation is based on several assumptions: (a) $\mathbf{B_0}$ is taken parallel to the z-direction. In a GARfield NMR setup, the magnet is originally designed such that the modulus of the magnetic field $\mathbf{B_0}$ in y–z plane is constant. This means that the direction of $\mathbf{B_0}$ itself varies along the z axis. However, in our GARfield NMR the surface coil is about 3 mm in diameter, consequently, the static magnetic field $\mathbf{B_0}$ can be taken to be parallel to the sample plane z-direction within the sensitive area. (b) The coating sample is homogeneous within the y–z plane. (c) The magnetic susceptibility of the sample and substrate are negligible, and therefore, the direction and magnitude of the $\mathbf{B_0}$ field do not change due to the presence of sample and substrate. We will show later that this assumption is quite realistic and simplify the calculations.

2.1. Spin dynamics in an inhomogeneous RF and static magnetic field

Spin voxels with a total magnetization M (M_x, M_y, M_z) are considered in a local rotating frame which rotates around $\mathbf{B_0}$ with a Larmor frequency $\omega_\mathbf{0}$ [rad/s]. For simplicity, we make the usual transformation using a transform matrix T [21,22]:

$$\begin{pmatrix} M^+ \\ M^- \\ M^0 \end{pmatrix} = T \cdot \begin{pmatrix} M_x \\ M_y \\ M_z \end{pmatrix} = \begin{pmatrix} 1 & i & 0 \\ 1 & -i & 0 \\ 0 & 0 & 1 \end{pmatrix} \cdot \begin{pmatrix} M_x \\ M_y \\ M_z \end{pmatrix}. \quad (2)$$

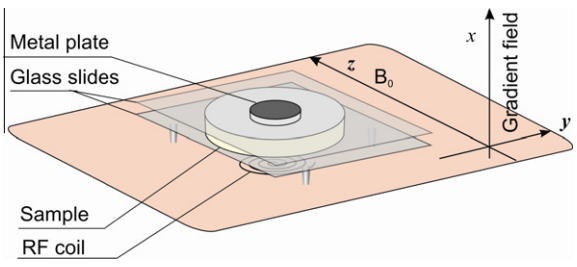

Fig. 1. Schematic illustration of the experimental MRI setup.

One of the advantages of this transformation is that the dephasing matrix with phase angle φ has only diagonal elements in case of free precession [23]:

$$R_\varphi = \begin{pmatrix} e^{i\varphi} & 0 & 0 \\ 0 & e^{-i\varphi}0 & \\ 0 & 0 & 1 \end{pmatrix}, \tag{3}$$

The evolution of the magnetization matrix due to an RF pulse can be written in the following form:

$$\begin{pmatrix} M^+(\tau_p) \\ M^-(\tau_p) \\ M_0(\tau_p) \end{pmatrix} = R(\phi,\alpha,\theta)\cdot \begin{pmatrix} M^+(0) \\ M^-(0) \\ M_0(0) \end{pmatrix}, \tag{4}$$

where τ_p [μs] is the pulse duration, ϕ [rad] the phase angle of the pulse, α [rad] the off-resonance angle and θ [rad] the effective flip angle. The off-resonance angle α is defined as the angle between the effective off-resonance field $\mathbf{B}_{eff} = \Delta\mathbf{B}_0 + \mathbf{B}_1$ and $\mathbf{B_1}$, $\cos\alpha = \frac{\mathbf{B_1}\mathbf{B_{eff}}}{|\mathbf{B_1}||\mathbf{B_{eff}}|}$, where $\mathbf{B_1}$ is the RF field produced by the coil. The off-resonance field is a result of the high magnetic field gradient and can be calculated by $\Delta\mathbf{B}_0 = \mathbf{G}\Delta x$, where $\mathbf{G}$ [T/m] is the static gradient field strength and Δx [μm] the perpendicular distance from the on-resonance slice. The effective flip angle θ is given by $\theta = \gamma|\mathbf{B_{Eff}}|\tau_p = \gamma\tau_p\sqrt{\Delta\mathbf{B}_0^2 + \mathbf{B}_1^2}$, in which γ represent the gyromagnetic ratio 267.5×10^6 rad·s^{-1}·T^{-1} for proton. The full rotation matrix can be calculated as follows [22,24]:

$$R(\phi,\alpha,\theta) = T, R_\phi, R_\alpha, R_\theta, R_\alpha^{-1}, R_\phi^{-1}, T^{-1}, \tag{5}$$

$$R_\phi = \begin{pmatrix} \cos\phi & -\sin\phi & 0sin\phi\cos\phi 0 \\ 0 & 0 & 1 \end{pmatrix}, \quad R_\alpha \begin{pmatrix} \cos\alpha & 0 & \sin\alpha \\ 0 & 1 & 0 \\ -\sin\alpha & 0 & \cos\alpha \end{pmatrix},$$

$$R_\theta \begin{pmatrix} 1 & 0 & 0 \\ 0 & \cos\theta & -\sin\theta \\ 0 & \sin\theta & \cos\theta \end{pmatrix}.$$

For a sequence $\theta_x - [\frac{t_e}{2} - \theta_y - \frac{t_e}{2} - echo]_n (n=1)$ with arbitrary flip angle θ, the spin density matrix evolution can be written as:

$$\mathbf{M} = \begin{pmatrix} M^+(t) \\ M^-(t) \\ M_0(t) \end{pmatrix} = R_\varphi\cdot R(\phi_y,\alpha,\theta)\cdot R_\varphi\cdot R(\phi_x,\alpha,\theta)\cdot \begin{pmatrix} M^+(0) \\ M^-(0) \\ M_0(0) \end{pmatrix}, \tag{6}$$

where ϕ_x and ϕ_y are 0 and $\pi/2$, respectively. Note that the off-resonance angle α and flip angle θ depend on the position of the voxel. The evolution can be divided into many coherence pathways [24], and the magnetization in the voxel is the sum over all possible pathways. Therefore, after the matrix multiplication, the expressions of $M^+(t)$ and $M^-(t)$ are extremely complicated. Fortunately, only those terms which are independent of the phase gained during the evolution period will contribute to the echo signal. In other words, only those terms not containing the variable φ contribute to the echo. Therefore, we can simply remove all the terms which contain the variable φ. After this step, $\mathbf{M}$ can be simplified [23]:

$$\mathbf{M} = \begin{pmatrix} M_x \\ M_y \\ M_z \end{pmatrix} = M_0 \begin{pmatrix} 2\cos^3\alpha\sin\alpha\sin^4\frac{\theta}{2} \\ -\cos^3\alpha\sin^2\frac{\theta}{2}\sin\theta \\ \frac{1}{2}(2\cos^4\alpha\cos^2\theta + 2\sin^4\alpha + \cos\theta\sin^2 2\alpha) \end{pmatrix}. \tag{7}$$

Now $\mathbf{M}$ describes the magnetization in a voxel in space having a certain off-resonance angle α and flip angle θ.

2.2. RF field of a surface coil

The $\mathbf{B_1}$ field produced by a single-turn circular coil can be calculated by:

$$\mathbf{B}_1 = \frac{\mu_0}{4\pi} I \oint \frac{\mathbf{r}\times \mathrm{dl}}{|\mathbf{r}|^3}, \tag{8}$$

where $\mu_0[T\cdot\frac{m}{a}]$ is the magnetic permeability of vacuum, I [A] is the current in the coil; dl is a coil element; $\mathbf{r}$ is the displacement vector from the element to the field point and the integral is over the current distribution in the coil. The $\mathbf{B_1}$ field of a circular surface coil with i turns is the sum of the $\mathbf{B_1}$ fields from the individual turns:

$$\mathbf{B}_{i,coil} = \frac{\mu_0}{4\pi} I \sum_i \oint_{l_i} \frac{\mathbf{r}\times \mathrm{dl_i}}{|\mathbf{r}|^3} = I\mathbf{b}_{coil}, \tag{9}$$

where $\mathbf{b}_{coil}$ is a constant related to the size and geometry of the coil. The $\mathbf{B_1}$ field of a surface coil with and without an aluminum plate (see Fig. 1) was simulated using a 2-dimensional model shown in Fig. 2. Since the RF coil of the setup has a symmetrical geometry, axial symmetry was used in the simulation. An oscillating external current was applied to the coil. The size of simulated domain was set much larger than the size of the coil to avoid boundary effects, because the domain boundaries were set to magnetic insulation. The aluminum plate was treated as an ideal metal conductor, and its boundary condition was set as magnetic insulation ($\mathbf{B} = 0$). We will show in Section 4.6 that these approximations are accurate enough for the simulation. The strength of the $\mathbf{B_1}$ field is calculated from $\mathbf{B} = \nabla\times\mathbf{A}$, where $\mathbf{A}$ is the vector potential.

2.3. The induced NMR signal

Assuming the magnetic moment of a certain voxel to be $\mathbf{M}$, the vector potential generated by this magnetic moment can be written as [25,26]:

$$\mathbf{A} = \frac{\mu_0}{4\pi}\frac{\mathbf{M}\times\mathbf{r}}{|\mathbf{r}|^3} \tag{10}$$

Using Stokes theorem, the surface integral of the magnetic flux density $\mathbf{B}$ is equal to the contour integral of the vector potential $\boldsymbol{A}$. So, the magnetic flux through the coil is:

$$\Phi_m = \iint_S \mathbf{B}\cdot\mathbf{n}\mathrm{dS} = \iint_S (\nabla\times\mathbf{A}\cdot\mathbf{n}\mathrm{dS} = \oint_l \mathbf{A}\cdot\mathbf{dl}. \tag{11}$$

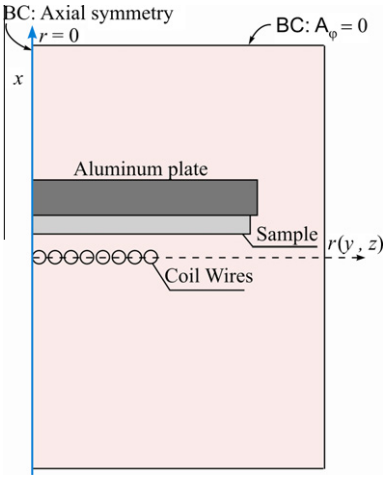

Fig. 2. Schematic overview of the $\mathbf{B_1}$ field simulation. "BC" refers to "boundary condition". Dimensions are not to scale.

The total magnetic flux captured by the coil $\Phi_{m,tot}$ is the sum of the flux penetrating through each coil turn i. Using Eq. (10), Eq. (11) becomes:

$$\Phi_{\mathrm{m,tot}} = \frac{\mu_0}{4\pi}\sum_i \oint_{\mathrm{l_i}} \frac{\mathbf{M}\times\mathbf{r}}{|\mathbf{r}|^3}\cdot \mathrm{d}\mathbf{l}_i = \frac{\mu_0}{4\pi}\sum_i \mathbf{M}\cdot\oint_{\mathrm{l_i}} \frac{\mathbf{r}\times \mathrm{d}\mathbf{l}_i}{|\mathbf{r}|^3} = \mathbf{M}\cdot\mathbf{b}_{coil}. \tag{12}$$

Because the same coil is used for transmission and receiving, $\boldsymbol{b}_{coil}$ can be calculated from Eq. (9) and Eq. (12) can be written as

$$\Phi_{\mathrm{m,tot}} = \mathbf{M}\cdot\frac{\mathbf{B}_{1,\mathrm{coil}}}{I} = \mathbf{M}\cdot\frac{\mathbf{B}_{1,\mathrm{coil}}}{I}, \tag{13}$$

where $\mathbf{B}_{1,\mathrm{coil,n}}$ is the normal component of $\mathbf{B}_{1,\mathrm{coil}}$, i.e., perpendicular to the coil surface. $\mathbf{B}_{1,\mathrm{coil}}$ can be replaced by $\mathbf{B}_{1,\mathrm{coil\ n}}$ because of other components will cancel out due to coil symmetry and a homogeneous sample parallel to the coil surface (assumption b in Section 2).

The precession of the magnetic moment $\mathbf{M}$ can be described as:

$$\mathbf{M}(t) = \begin{pmatrix} M_x\cos(\omega t+\varphi) \\ -M_y\sin(\omega t+\varphi) \\ M_z \end{pmatrix}. \tag{14}$$

The precession of the magnetic moment $\mathbf{M}$ in a certain voxel will create a fluctuating magnetic flux in the receiving coil, and the induced voltage (NMR signal) is proportional to the fluctuation rate $\frac{d\mathbf{M}(t)}{dt}$:

$$V = \frac{d\Phi_{m,tot}}{dt} = \frac{\mathbf{B}_{1,\mathrm{coil,n}}}{I}\cdot\frac{d\mathbf{M}(t)}{dt} = \frac{\mathbf{B}_{1,\mathrm{coil,n}}}{I}\cdot\omega\begin{pmatrix} -M_x\sin(\omega t+\varphi) \\ -M_y\cos(\omega t+\varphi) \\ M_z \end{pmatrix}. \tag{15}$$

So, NMR signals at the x and y channels of the NMR receiver are:

$$V_x = \frac{\mathbf{B}_{1,\mathrm{coil,n}}}{I}\omega \mathrm{M}_x, \tag{16}$$

$$V_y = \frac{\mathbf{B}_{1,\mathrm{coil,n}}}{I}\omega \mathrm{M}_y. \tag{17}$$

These signals are originating from the magnetic moment of a voxel, and are detected by the receiving coil. Note that since the initial magnetization $\mathbf{M_0}$ itself is proportional with $\mathbf{B_0}$ (or Larmor frequency ω), V_x and V_y are proportional to ω^2. The evolution of M_x and M_y following the RF pulse sequence can be computed by the spin density matrix formalism, i.e., Eq. (7). The overall signal at a certain Larmor frequency can be calculated by integrating the signal density of each voxel (V_x and V_y) over y–z planes (Fig. 2) parallel to the surface coil:

$$V_{x,tot} = \int_0^\infty \frac{\mathbf{B}_{1,\mathrm{coil,n}}}{I}\omega 2\pi R M_x(t)dR, \tag{18}$$

$$V_{y,tot} = \int_0^\infty \frac{\mathbf{B}_{1,\mathrm{coil,n}}}{I}\omega 2\pi R M_y(t)dR, \tag{19}$$

$$V_{tot} = \sqrt{V_{x,tot}^2 + V_{y,tot}^2}, \tag{20}$$

where R is the distance from the symmetry axis of the surface coil in the y–z plane.

All parameters used in the simulation are specified in Table 1.

3. Experimental

3.1. NMR

The NMR imaging setup used in the present study consists of a GARfield magnet and a home-made acquisition system which has been described elsewhere by Kopinga and Pel [27]. One of the advantages of the GARfield approach is that the sample can be placed directly on top of a surface coil, which yields an optimal signal-to-noise ratio, but at the cost of homogeneity of the $\mathbf{B_1}$ field. The static field $\mathbf{B_0}$ of the magnet at the position of the sample is 1.5 T, and the gradient G is 40 T/m. All the signal profiles were measured with a pulse sequence $\theta_x - [t_e/2 - \theta_y - t_e/2 - echo]_n$. A pulse duration of 1 μs and an inter-echo time t_e of 100 μs were specified in all measurements. The theoretical spatial resolution that can be achieved by this inter-echo time setting is about 7 μm. Each signal profile was averaged 2048 times and the long delay between two subsequent pulse sequences was set to 0.5 s.

3.2. Sample

NMR measurements were performed on layers of silicon. The silicon was sandwiched between two glass slides with thickness of about 100 μm, and cured at room temperature for 48 h before the measurements. For the measurements with metal plates, a metal plate with a diameter of about 8 mm and thickness of about 600 μm was put directly on top of the glue sandwich, as shown in Fig. 1. Unless otherwise stated, the distance from metal plate to surface coil was kept at 500 μm in both the simulations and the experiments. In the following discussion the silicon sample covered by an aluminum plate and the sample without aluminum plate will be referred to as Al-glue and glass-glue, respectively.

In order to illustrate the possibility to investigate a dynamic process on a metallic substrate using our GARfield MRI system, the curing process of an epoxy-amine system, which is a typical polymer coating for metallic substrates, was chosen as an example. The epoxy resin used was EPIKOTE 828 [28], which is a liquid epoxy resin with an aromatic backbone without solvent. A phenalkamine, Cardolite LX-5206, was used as curing agent. The two components were mixed in for 5 min and subsequently applied on either glass or aluminum substrates for the measurements. The molar ratio of the functional groups for the two components was 1:1 for all samples. Two samples were prepared for comparison, glass–epoxy and Al-epoxy. The first sample was prepared by sandwiching the epoxy polymer between two glass slices, and the second sample was prepared by sandwiching the polymer between one glass slice and one aluminum plate. The thickness of the polymer coatings was about 200 μm.

4. Results and discussion

4.1. Magnetic susceptibility effects

As mentioned in Section 1, the artifacts induced by metallic substrates may originate from either magnetic susceptibility differences or eddy currents. The magnetic susceptibility is given by $\chi = \frac{\partial \mathbf{M}}{\partial \mathbf{H}}$ [29], in which $\boldsymbol{H}$ is the applied magnetic field, and $\mathbf{M}$ is the induced magnetization of the material. Susceptibility differences within the sample will lead to a faster T_2 relaxation in the time domain. Although the effect of field inhomogeneities can be refocused or eliminated at the center of a Hahn spin echo, susceptibility effects can change the local Larmor frequency and therefore hamper the transformation from the frequency to the spatial domain. As a consequence, the resulting images are distorted.

Table 1
Parameters for the simulation.

Category	Symbol	Quantity	Units	Comments
RF pulse	I	Electric current	A	$I = I_0 \sin(\omega_0 t)$, I_0 and ω_0 are the amplitude and frequency of the alternating current
	$\omega_0 2\pi$	Frequency of the current	Hz	62.5 MHz
	τ_p	Pulse duration	μs	1.5 μs
Static magnetic field	$\mathbf{B_0}$	Static magnetic field	T	1.5 T
	$\mathbf{G}$	Static field gradient	T/m	40 T/m
	x	Distance from the coil	μm	The coordinate system is defined in Fig. 1
	x_0	x coordinate of the on-resonance slice	μm	
	Δx	Distance from the on-resonance slice	μm	$\Delta x = x - x_0$
Spin evolution	γ	Gyro-magnetic ratio of proton	rad/(s T)	267.5×10^6
	$\Delta\mathbf{B_0}$	Off-resonance field	T	$\Delta\mathbf{B}_0 = \mathbf{G} \cdot \Delta x$
	$\mathbf{B}_{1,\mathrm{coil,n}}$	Normal component of the RF field	T	
	B_{eff}	Effective RF field	T	$\mathbf{B}_{\mathrm{eff}} = \Delta\mathbf{B}_0 + \mathbf{B}_1$
	θ_{eff}	Effective flip angle	rad	$\theta = \gamma \cdot \lvert\mathbf{B}_{\mathrm{eff}}\rvert \cdot \tau$,
	α	Off-resonance angle	rad	The angle between the effective field $\mathbf{B}_{\mathrm{eff}}$ and $\mathbf{B}_1$, $\cos\alpha = \frac{\mathbf{B}_1 \cdot \mathbf{B}_{eff}}{\lvert\mathbf{B}_1\rvert\lvert\mathbf{B}_{eff}\rvert}$
Coil geometry and properties	n	Turns of the surface coil		8
	d	Diameter of the coil wire	μm	180 μm
	D	Diameter of the coil	mm	3.2 mm
	σ	Electric conductivity of copper	S/m	5.96×10^7 S/m

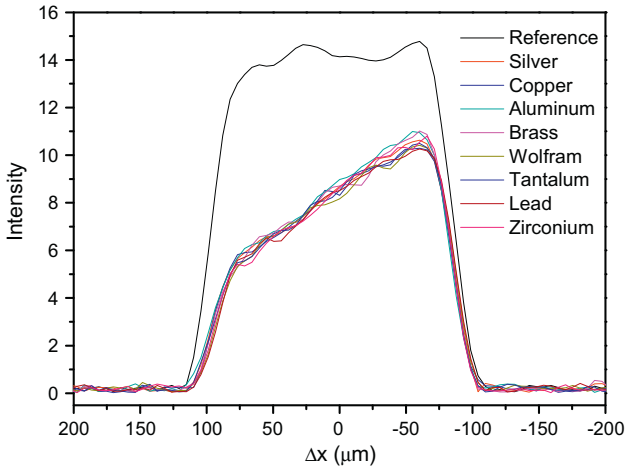

Fig. 3. NMR signal profile of silicon in the presence of different metal plates. The sample was sandwiched between two glass slides, and a metal plate was placed on the top, as shown in Fig. 1. The diameter of all metal plates was 8 mm.

Fig. 3 shows the NMR signal profiles of a silicon sample in the presence of different metal plates. A reference signal recorded without metal plate is also presented for comparison. It is very interesting to notice that the signal profiles of the sample covered by different metal plates are quite similar, even though the susceptibility and the electrical resistivity of these materials vary over more than one order of magnitude (Table 2).

Susceptibility induced artifacts have been studied extensively, and it is well understood that the magnitude of this effect scales with field strength and material susceptibility [12,13,30–33]. The maximum field perturbation induced by susceptibility of the materials can be roughly estimated by the following formula:

$$\Delta B \approx \chi |\mathbf{B}_0|. \tag{21}$$

An object with $\chi = 1 \times 10^{-6}$ (1 ppm) produces a maximum resonance frequency perturbation of about ±1 ppm in the surrounding space. In practice, the object's geometry (shape, size, etc.) will also change the actual value of ΔB. The non-magnetic materials with $\chi \ll 1$ used in our experiments can only produce very small fractional perturbations in an applied field. This perturbation is negligible in the strong gradient field (40 T/m). Tantalum, for instance, with $\chi = 178 \times 10^{-6}$, produces a perturbation of about 11 kHz in a $\mathbf{B_0}$ field of 62.5 MHz. This perturbation corresponds to an error of about 5 μm in space, which is comparable to the resolution of our setup. Therefore, no visible frequency shift has been observed among the signal profiles obtained with the different metals (Fig. 3). These results show that on the one hand, the susceptibility of the different metal plates has only a small effect (5 μm) on the NMR profiles as long as the plates are non-magnetic. On the other hand, the difference in the conductivity of these metal plates also appears to have a negligible effect. The penetration depth of the RF field is small compared to the geometry of the metal plates, and all plates perfectly screen the RF field in the experiments. These results validate the boundary condition of 'magnetic insulation' for the aluminum plate in the $\mathbf{B_1}$ field calculations in Section 2.2.

Table 2
Susceptibility and electrical resistivity of selected weakly magnetic materials[a].

Material	Silver	Lead	Copper	Aluminum	Wolfram	Zirconium	Tantalum
Magnetic susceptibility[b] (10^{-6})	−24	−15.8	−9.63	20.7	77.2	109	178
Electrical resistivity (10^{-8} Ω m)	1.47	20.6	1.75	2.83	5.3	45.0	13.5

[a] The susceptibility and resistivity of brass depend highly on its composition, therefore no unambiguous literature value has been found.
[b] All the susceptibility values are for volume susceptibility. SI units were used to calculate these dimensionless numbers.

4.2. The RF field

We have shown that the magnetic susceptibility has a relatively minor effect on the GARfield NMR profiles. This section mainly focuses on the effect of eddy currents in a metallic substrate. To understand this effect, the complete NMR profiles with and without a metal plate were simulated numerically. The first step is to simulate the RF field of the surface coil. The GARfield NMR setup is characterized by strong inhomogeneities, not only in the static magnetic field, but also in the RF field of the surface coil. In the experiments, the actual current in the coil is difficult to measure. In order to relate the simulation results to experimental power level inputs, the currents of the transmitter coil used for the simulation are calibrated as follows. First, the experimental power level is adjusted such that the signal intensity of the on-resonance slice has a maximum. Second, the intensity of the on-resonance slice is simulated for a broad range of hypothetical currents (10^{-3}–10^{3} A). Third, the currents yielding a maximum of the simulated intensities are assumed to be identical to the corresponding experimental currents, which occur at power levels of 41 dBm and 46 dBm for the glass-glue sample and Al-glue sample, respectively. Finally, all the currents used for the simulation are presented in dBm in order to compare with the experimental values.

In order to quantify the flip angle of the spins in each voxel of the sample, the RF field of the coil was simulated. Fig. 4 shows plots of the z component of the $\mathbf{B_1}$ field strength as a function of position (R, x). This component has a maximum value at $R = 0$, and reaches a minimum (negative value) at the edge of the coil ($R = 1.6$ mm). It is interesting to notice that in the near vicinity of the coil, $\mathbf{B}_{1,\mathrm{coil,n}}$ is constant for different slices at $R \approx 1.3$. Comparison of Fig. 4a and b shows that when an Al plate is located at$x = 500$ μm, $\mathbf{B}_{1,\mathrm{coil,n}}$ is strongly suppressed in the sample volume.

4.3. NMR signal from the voxels

Quantitative information about the signal distribution in a sample slice (y–z plane) is important for understanding the NMR profiles. It would also be interesting to know the most sensitive regions of the surface coil. However, in experiments it is only possible to obtain the overall intensity from a sample slice where all the spins precess at the same Larmor frequency, and hence no detailed information about the distribution of the NMR signal within this slice can be obtained. An advantage of the present simulation is that it is possible to calculate the signal intensity in each voxel and the intensity distribution over the sample volume. Fig. 5 shows the NMR signal distribution along the radial direction of the coil. The intensity for each parallel slice is represented by a different curve. For a surface coil with a diameter of 3.2 mm, the sensitive region is located within a diameter of about 2 mm. The signal from the sample voxels on the axial-symmetry axis is most sensitive to the distance x, and this sensitivity decreases with increasing distance from the symmetric axis, R. The signal intensity of the Al-glue sample is systematically lower than that of the glass-glue sample. At $R \approx 1.3$ mn, the signal is almost zero for both samples. At $R \approx 1.5$ mn, close to the edge of the surface coil, the NMR signal arises again slightly for both samples, and the signal of the Al-glue sample is a bit more pronounced than that of the glass-glue sample. This is explained by the $\mathbf{B_1}$ field distribution profiles plotted in Fig. 4, which shows a constant and small $\mathbf{B}_{1,\mathrm{coil,n}}$ values at $R \approx 1.3$ mn, and negative $\mathbf{B}_{1,\mathrm{coil,n}}$ value at $R \approx 1.5$ mm.

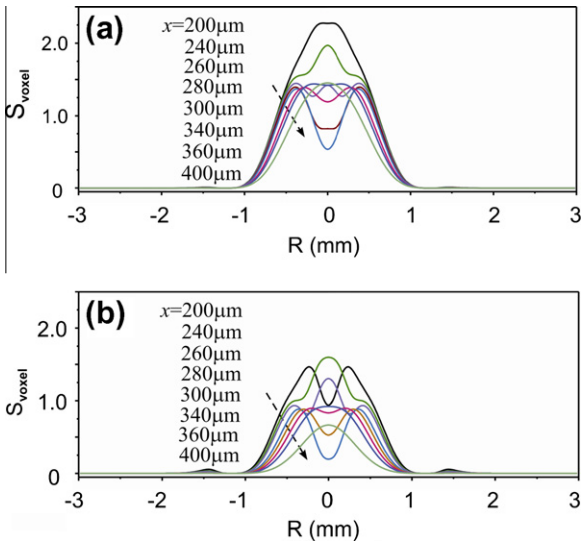

Fig. 5. NMR signal distribution along the radial direction of the coil. Each curve in the figure represents the NMR signal in the surface coil produced by spins in a sample slice parallel to the coil. The distances between the slices and the coil are indicated in the figures. The slice at position of $x = 310$ μm is on-resonance. The RF power levels which are chosen to correspond to the experimental situation, which will be addressed in Section 4.4, are 41 dBm and 46 dBm for (a) glass-glue and (b) Al-glue sample, respectively.

4.4. The NMR intensity from the on-resonance slice

In the previous section, we showed the distribution of the NMR signal from sample voxels with a y–z slice. The present section will focus on the integral NMR signal of the entire sample slice. To

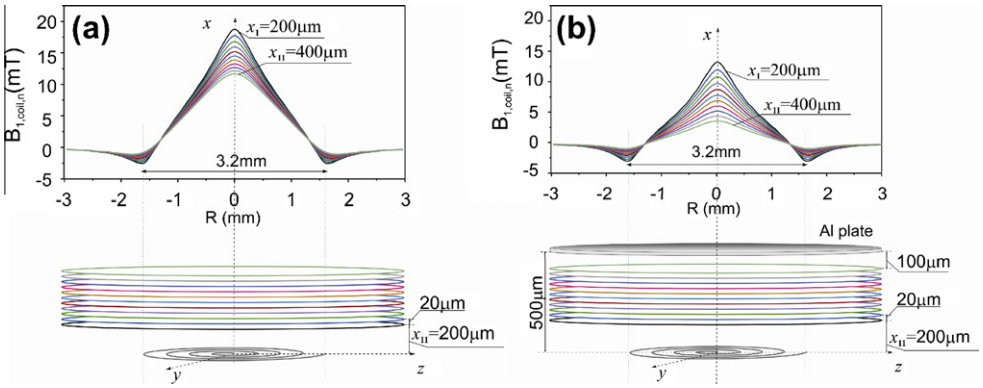

Fig. 4. Simulated z component of the $\mathbf{B_1}$ field distribution. (a) glass-glue; (b) Al-glue with an Al plate placed at $x = 500$ μm. $\mathbf{B}_{1,\mathrm{coil,n}}$, which is the normal component of $\mathbf{B}_{1,\mathrm{coil}}$, is plotted against R. Different curves in the figures represent $\mathbf{B_1}$ field distributions in different slices parallel to the coil. The top curve corresponds to the bottom slice in the lower part of each figure. Eleven slices at position of $x = 200, 220, 240\ldots400$ μm are presented.

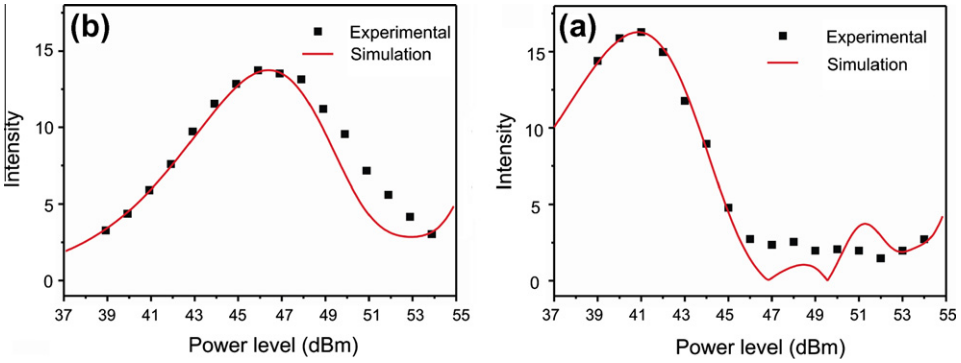

Fig. 6. Experimental and simulated on-resonance slice intensity plotted against the power input. (a) glass-glue; (b) al-glue.

calculate the intensity from an on-resonance slice, the sample was divided into small voxels, and V_x and V_y were calculated independently using Eq. (16) and Eq. (17). Next, the signal at the x and y channels of the receiver ($V_{x,tot}$, $V_{y,tot}$) was calculated by integrating V_x and V_y over the entire slice using Eq. (18) and Eq. (19). Finally, the overall signal was calculated using Eq. (20). Fig. 6 shows the experimental and simulated intensity from the on-resonance slice versus the power level input to the coil. When the power level is below 45 dBm, the simulated results fit the experimental results very well. At higher power levels, some deviations occur between the simulated and experimental results. One of the possible reasons may be the heating of the coil by the RF pulse. At higher power levels, relatively more energy is dissipated in the coil, which leads to a weaker RF field than in the simulations.

Fig. 6 also shows that the peak intensity of the Al-glue sample (Fig. 6b) is somewhat lower than that of the glass-glue sample. The peak intensity occurs at about 41 dBm for the glass-glue sample, whereas for the Al-glue sample the maximum is at 46 dBm, which means that to measure a polymer coating on a metallic substrate, more RF power is needed to reach the maximum intensity. This result shows that it is possible to perform MRI of a polymer coating on a metallic substrate, but with more power input and less signal compared to that on a non-metallic substrate. Further it is demonstrated that the behavior of the signal can be predicated with a reasonable accuracy.

4.5. Excitation bandwidth of RF pulses in GARfield NMR

In the previous section, we have simulated the on-resonance slice intensity at different RF power levels. However, the quantitative relation between NMR intensity and frequency offset, $\Delta f = \gamma G \Delta x$, is not trivial. This section will focus on how the NMR intensity changes with the frequency offset.

In homogeneous-field or weak-gradient NMR experiments, off-resonance effects are generally not considered explicitly because the frequency offset produced by chemical shift anisotropy, dipolar–dipolar interactions and/or static gradients, etc., is usually within the bandwidth of the RF pulse. In the GARfield approach, however, a wide frequency distribution is produced because of the strong gradient, and the off-resonance effect has to be taken into account. In order to study the off-resonance effect on the NMR signal, the distance between sample and coil was kept constant and the whole assembly was moved along the direction of gradient (along the x axis). In this way, the RF field strength experienced by each spin is kept constant, and only the strength of the $\mathbf{B_0}$ field is changed. In this way, we actually sweep the Larmor frequency of the spins. The intensity of the sample slice at a distance of $x = 310$ μm from the coil, which is on-resonance when the stage position $\Delta x = 0$ μm, is plotted against the displacement of the stage in Fig. 7. The distance between the Al plate and RF coil was about 500 μm for the Al-glue sample. Because the experimental value of the pulse length was set to 1 μs for all the measurements (see Section 3.1), we also assumed an ideal 1 μs square pulse in the simulation. It results in an excitation profile with a sinc function lineshape in the frequency domain. For both samples, the experimental curves are significantly narrower than the curves simulated with a pulse duration of 1 μs. This suggests that in the experiments the excitation frequency range of the RF pulse is narrower than the theoretical excitation range of an ideal 1 μs square pulse. This can be understood from the fact that the actual RF pulse is not an ideal square pulse, and its effective duration is longer than 1 μs due to the electromagnetic response of the coil system. A longer pulse in the time domain will result in a narrower excitation range in the frequency domain. In order to confirm this, we also simulated the profiles with longer RF pulse durations. Best matches were found for a pulse duration of 1.5 μs, which are shown in Fig. 7a and b. This indicates that in our experiments the actual pulse duration was about 1.5 μs instead of 1 μs. Therefore, a pulse duration of 1.5 μs was used for all the simulations in this work in order to be consistent with the experimental results. Besides the pulse length, the shape of the curves in Fig. 7 also depends on the strength (or amplitude) of the pulse. For the glass-glue sample, a minimum is observed at $x = 0$ μm, whereas the Al-glue sample shows only a single peak. This is caused by the fact that, for the same RF power level of 42 dBm, the actual RF fields are not the same for these two samples because of the eddy currents in the Al plate. Increasing the RF power level for the Al-glue sample would result in a similar curve as for the glass-glue sample.

4.6. Simulation of complete NMR profiles

From the results presented in the previous section, it is known that the actual value of the pulse length in the experiments is 1.5 μs. In this section, we will simulate the NMR profiles in the entire frequency range with a pulse length of 1.5 μs. In a homogeneous $\mathbf{B_1}$ field, e.g., the $\mathbf{B_1}$ field of a volume coil, the flip angle is well defined. However, the $\mathbf{B_1}$ field of a surface coil used in GARfield NMR is very inhomogeneous, as shown in Fig. 4. The flip angle and resonance offset vary strongly across the sample. This makes it challenging to explain the NMR signals. The presence of the metal plate distorts the $\mathbf{B_1}$ field further, and makes the situation even more complex. In order to quantitatively determine the effect of a metal plate on the NMR signal profiles in an inhomogeneous $\mathbf{B_1}$ and $\mathbf{B_0}$ field, the first echo generated by an O–W sequence was simulated by considering the flip angle distribution and off-resonance effects. Fig. 8 shows a comparison between the experimental and simulated NMR signal profiles obtained at different RF power levels. Despite the assumptions that have been made in the simula-

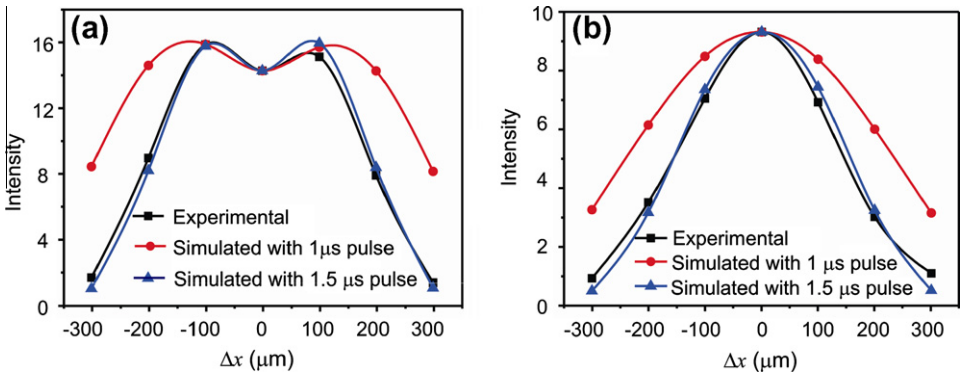

Fig. 7. Off-resonance effects on the NMR signals. The experimental results are obtained by moving the whole stage (including sample and coil) through the $\mathbf{B_0}$ field. Intensities of the slice at a distance of 310 μm from the coil surface are plotted against the position of the stage. At a stage position of $\Delta x = 0$ μm, the recorded slice is on-resonance. The power level used was 42 dBm for all the measurements on both samples, (a) glass-glue; (b) Al-glue. The distance x between Al plate and coil surface was 500 μm.

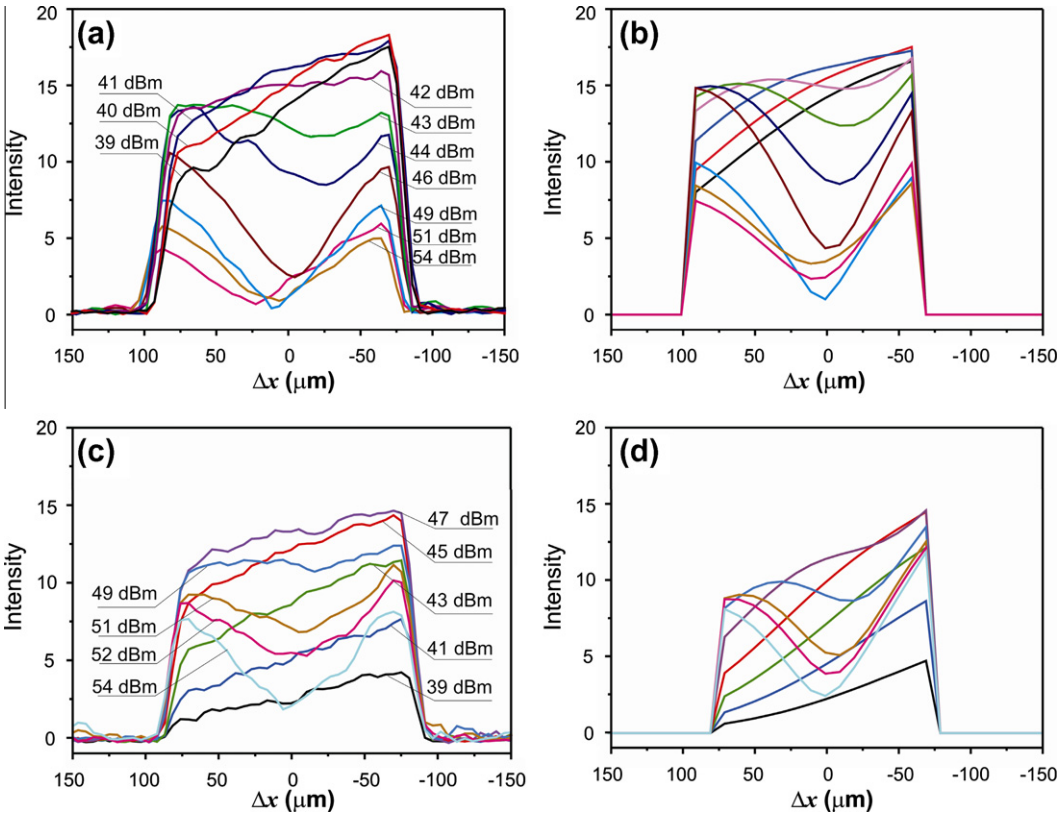

Fig. 8. Experimental and simulated NMR signal profiles at different power levels. The pulse length was 1.5 μs for all measurements and simulations. The x-coordinate was chosen such that the on-resonance slice corresponds to $\Delta x = 0$ μm. (a) and (c) are the experimental results for the glass-glue and Al-glue samples, respectively; (b) and (d) are the simulation results for (a) and (c), respectively.

tion, as discussed in Section 2, the simulated results agree very well with the experimental results. For the glass-glue sample, the NMR intensity increases as the power level increases from 39 dBm to 41 dBm, and then the intensity decreases as the power level increases further. A broad minimum centered at the on-resonance slice ($\Delta x = 0$ μm) is observed when the power level is higher than 46 dBm. A similar phenomenon is also observed for the Al-glue sample. For this sample, the power level at maximum intensity is 47 dBm, which is about four times higher. This result clearly shows how the metal plate affects the NMR profiles. Due to the generated eddy currents in the metal plate, the actual RF field in the sample volume is attenuated. So, more power is needed to compensate this eddy current effect and obtain a comparable RF field. These results demonstrate that for a correct interpretation of an NMR signal profile, a calibration with the same sample geometry and the same RF power is necessary. Different RF power levels can result in completely different profiles.

5. Curing process of an epoxy/phenalkamine system

To demonstrate the application of GARfield NMR to polymer coatings on metal substrates, the curing processes of epoxy/phenalkamine on metallic and non-metallic substrates at room temperature are compared. Fig. 9 shows the NMR profiles of these epoxy coatings on different substrates. For both glass–epoxy and Al-epoxy samples, the coatings remain homogeneous throughout the curing process and no phase separation occurs. In order to

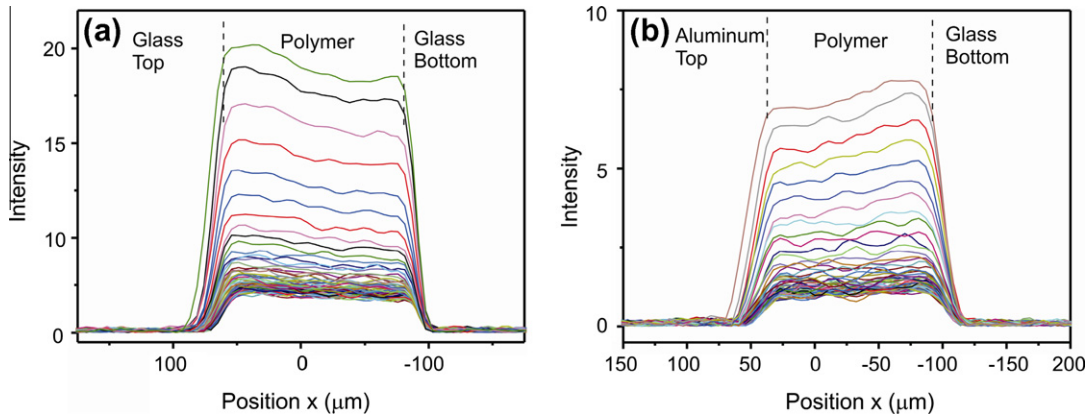

Fig. 9. NMR profiles of an epoxy coating on two different substrates during the curing process. (a) glass–epoxy; the epoxy coating was sandwiched between two glass slices. (b) Al-epoxy; the epoxy coating was sandwiched between a glass slice at the bottom and an aluminum plate on the top. The profiles were recorded consecutively and the measurement time for each profile was 21 min.

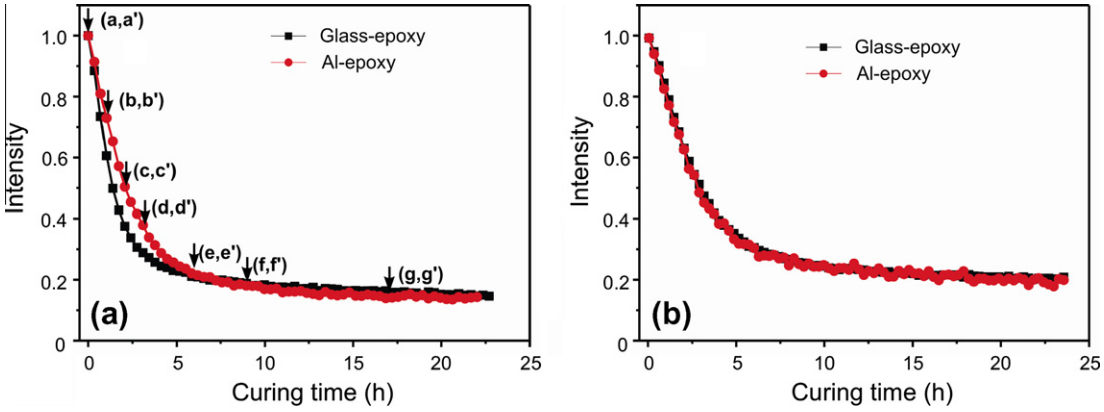

Fig. 10. Integrated NMR signal intensity plotted against curing time. The signals were recorded with (a) 1024 echoes and (b) 1 echo. For both samples, the intensities were normalized to the intensity of the first profile. $a, a', \ldots, g, g'$ are the selected times for the T_2 relaxation analysis presented in Fig. 11. The characters with primes refer to the Al-epoxy sample, and the letters without primes refer to the glass–epoxy sample.

investigate the effect of the substrate on the curing rate, the total signal intensity of the whole layer is plotted against the curing time in Fig. 10. Fig. 10a shows the NMR signal change with curing time recorded with an O–W sequence with 1024 echoes. It is interesting to notice that in the initial stage the curing rate of the glass–epoxy sample is higher than that of the Al-epoxy sample. After about 5 h, the curing process slows down and continues at a very low rate. A possible explanation for the different curing rates of these two samples is the difference in thermal conductivity of the glass and aluminum substrates. It is well known that the strong RF pulses may heat up the coil and the sample. To investigate this, we measured the temperature of the samples under experimental conditions by inserting a thermocouple into the polymer coating. At room temperature of 22.5 °C, 1024 echoes and an inter-echo delay of 100 μs, the coating temperature was 23.5 °C and 25.5 °C for the Al-epoxy and the glass–epoxy sample, respectively. The actual temperature in the Al-epoxy sample is lower than in the glass–epoxy sample. Therefore the curing rate of the Al-epoxy sample is slower. Obviously, the aluminum plate is a better sink for the excess heat. In order to minimize the heating effect of the RF pulses, we reduced the number of pulses. The NMR signal was then recorded with 1 echo instead of 1024 echoes, and the temperature of these two samples appeared to remain at room temperature, as measured by the thermocouple inserted in the sample. The results are plotted in Fig. 10b, which shows that both samples now cured at the same rate.

T_2 relaxation analysis can provide valuable information about the molecular dynamics of polymers. To compare the T_2 relaxation behavior of the epoxy samples on different substrates, 1024 echoes were recorded for each measurement. The signal decays (T_2 relaxation) were fitted using a continuous T_2-fitting procedure [34,35]. Fig. 11 shows the T_2 relaxation time distribution of both samples during the curing process. The horizontal axis represents the T_2 relaxation time and vertical axis gives information about the population of spins with that T_2 relaxation time. At the first time point ((a), (a′)), there are apparently four components with different relaxation times for both samples. With increasing curing time, T_2 of all components in both samples decreases, meaning that the whole system becomes more rigid. At the time points (c, c'), the fast relaxation components of both samples disappear and only three components are visible in the detected time range. From time (d, d') onwards, only two rigid components with short T_2 are left, and the T_2 relaxation times decrease continuously with curing time. It is outside the scope of this paper to go into details of the chemical process of this very specific example, but by combining the relaxation information with other analytical techniques, e.g., FTIR, DSC, etc., valuable information about the reaction mechanisms may be obtained. Comparing Fig. 11a and b, one observes that the T_2 relaxation times of the glass–epoxy sample are apparently longer than those of the Al-epoxy sample. As discussed before, this can be explained by the faster curing process of the former sample because of heating by the RF pulses. Also in these

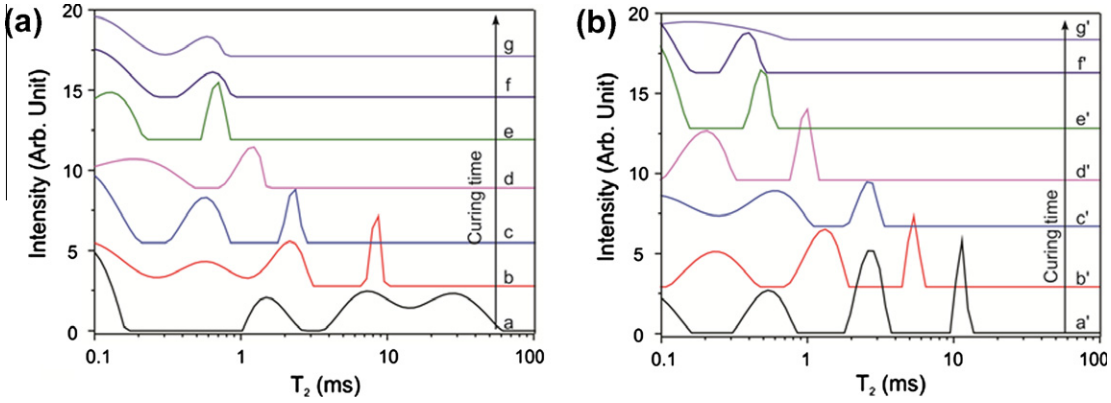

Fig. 11. T_2 relaxation times of (a) the glass–epoxy sample and (b) the Al-epoxy sample at different stages of the curing process. $a, a', \ldots, g, g'$ correspond to the times indicated by the arrows in Fig. 10a.

measurements, one can reduce the number of echoes to minimize the heating effect of the RF pulses. However, this may conflict with the detection of T_2 components which requires more echoes. A possible solution is to increase the long delay (or recycle delay), but at the price of longer measuring time.

6. Conclusions

The effects of a metallic substrate on high-spatial resolution NMR imaging profiles of coating films were studied from both experimental and theoretical point of view. The excellent agreement between the simulated and measured NMR profiles demonstrates that the simulated $\mathbf{B_1}$ field distribution of the surface coil and the NMR signal intensity calculations presented in Section 2 accurately describe the spin dynamics of GARfield NMR in extremely inhomogeneous $\mathbf{B_1}$ and $\mathbf{B_0}$ fields.

The susceptibility and eddy current effect of non-paramagnetic metallic substrates were evaluated. Both experiments and theory revealed that, for non-paramagnetic metals, the effect of susceptibility difference on MRI profiles is negligible in the strong static field gradient. The difference in conductivity of the metallic substrates does not affect the MRI profiles. However, the eddy currents produced by the metal plates can significantly change the $\mathbf{B_1}$ field distribution in the sample volume compared to the non-metallic substrates. The $\mathbf{B_1}$ field distribution around the surface coil was simulated with and without the presence of an aluminum plate. The complete GARfield NMR profiles were simulated by fully considering the inhomogeneity of the $\mathbf{B_1}$ field and off-resonance effects. The off-resonance effect in GARfield NMR is also discussed in detail in terms of the excitation profile of the RF pulse. In practice, the RF pulse length is larger than the length of the hard pulse generated by the RF power amplifier. This leads to a narrower excitation frequency range than that produced by the theoretical calculations.

Finally, as an example, the curing processes of an epoxy/phenalkamine system on aluminum and glass substrates were compared. To measure a comparable NMR signal on metallic substrates, more RF power is needed. Moreover, the heating effect of the RF pulses may have to be taken into account when comparing the NMR data measured on different substrates. This study may contribute to the feasibility of the NMR imaging of polymer coatings on metal substrates, which is important for the coating industry.

Acknowledgments

This project is funded by DPI, TU/e and TNO. The authors thank Hans Dalderop and Jef Noijen for technical support and assistance.

References

[1] J. Mitchell, P. Blümler, P.J. McDonald, Prog. Nucl. Magn. Reson. Spectrosc. 48 (2006) 161.
[2] P.J. McDonald, B. Newling, Rep. Prog. Phys. 61 (1998) 1441.
[3] B. Blümich, J. Perlo, F. Casanova, Prog. Nucl. Magn. Reson. Spectrosc. 52 (2008) 197.
[4] P.M. Glover, P.S. Aptaker, J.R. Bowler, E. Ciampi, P.J. McDonald, J. Magn. Reson. 139 (1999) 90.
[5] S.J.F. Erich, O.C.G. Adan, L. Pel, H.P. Huinink, K. Kopinga, Chem. Mater. 18 (2006) 4500.
[6] S.J.F. Erich, J. Laven, L. Pel, H.P. Huinink, K. Kopinga, Prog. Org. Coat. 52 (2005) 210.
[7] S.J.F. Erich, J. Laven, L. Pel, H.P. Huinink, K. Kopinga, Appl. Phys. Lett. 86 (2005) 134105.
[8] S.J.F. Erich, H.P. Huinink, O.C.G. Adan, J. Laven, A.C. Esteves, Prog. Org. Coat. 63 (2008) 399.
[9] S.J.F. Erich, J. Laven, L. Pel, H.P. Huinink, K. Kopinga, Prog. Org. Coat. 55 (2006) 105.
[10] J. Hua, R.A. Fox, J. Magn. Reson. Imaging 6 (1996) 264.
[11] J.A. Malko, J.C. Hoffman, P.J. Jarrett, Radiology 173 (1989) 563.
[12] C.R. Camacho, D.B. Plewes, R.M. Henkelman, J. Magn. Reson. Imaging 5 (1995) 75.
[13] J.F. Schenck, Med. Phys. 23 (1996) 815.
[14] K.M. Lüdeke, P. Röschmann, R. Tischler, Magn. Reson. Imaging 3 (1985) 329.
[15] M. Alecci, P. Jezzard, Magn. Reson. Med. 48 (2002) 404.
[16] H. Graf, G. Steidle, U.A. Lauer, F. Schick, Med. Phys. 32 (2005) 337.
[17] H. Graf, U.A. Lauer, A. Berger, F. Schick, Magn. Reson. Imaging 23 (2005) 493.
[18] E.D. Ostroff, J.S. Waugh, Phys. Rev. Lett. 16 (1966) 1097.
[19] Y.Q. Song, J. Magn. Reson. 157 (2002) 82.
[20] T. Graf, O. Schalli, A. Furrer, P. Marty, in: COMSOL Conference Milan, 2009.
[21] C.P. Slichter, Principles of Magnetic Resonance, Springer-Verlag, Berlin, New York, 1990 (3rd enl. and updated ed.).
[22] M.H. Levitt, Spin Dynamics: Basics of Nuclear Magnetic Resonance, second ed., John Wiley & Sons, New York, 2008.
[23] M.D. Hürlimann, J. Magn. Reson. 148 (2001) 367.
[24] R.R. Ernst, G. Bodenhausen, A. Wokaun, Principles of Nuclear Magnetic Resonance in One and Two Dimensions, Clarendon Press, Oxford, 1987.
[25] F. Bălibanu, K. Hailu, R. Eymael, D.E. Demco, B. Blümich, J. Magn. Reson. 145 (2000) 246.
[26] J.R. Reiz, F.J. Milford, R.W. Christy, Foundations of Electromagnetic Theory, fourth ed., Addison-Wisley, Reading, 2008.
[27] K. Kopinga, L. Pel, Rev. Sci. Instrum. 65 (1994) 3673.
[28] A. Foyet, T.H. Wu, A. Kodentsov, L.G. Van der Ven, G. De With, R.A. Van Benthem, ECS Trans. 25 (2010) 31.
[29] R.K. Wangsness, Electromagnetic Fields, second ed., John Wiley and Sons, New York, 1986.
[30] N.J. Kagetsu, A.W. Litt, Radiology 179 (1991) 505.
[31] M. Mößle, S.-I. Han, W.R. Myers, S.-K. Lee, N. Kelso, M. Hatridge, A. Pines, J. Clarke, J. Magn. Reson. 179 (2006) 146.
[32] M. O'Donnell, W.A. Edelstein, Med. Phys. 12 (1985) 20.
[33] T. Sumanaweera, G. Glover, S. Song, J. Adler, S. Napel, Magn. Reson. Med. 31 (1994) 40.
[34] Y.Q. Song, L. Venkataramanan, M.D. Hürlimann, M. Flaum, P. Frulla, C. Straley, J. Magn. Reson. 154 (2002) 261.
[35] L. Venkataramanan, S. Yi-Qiao, M.D. Hurlimann, IEEE Trans. Signal Process. 50 (2002) 1017.